Journal of Water Process Engineering 59 (2024) 105074

Contents lists available at ScienceDirect

Journal of Water Process Engineering

journal homepage: www.elsevier.com/locate/jwpe

Interfacial electron redistribution in 2D/3D $MoS_2/CuBi_2O_4$ p-n heterojunction for visible light assisted reduction of Cr(VI) and oxidation of antibiotics

Olalekan C. Olatunde [a,b], Tunde L. Yusuf [c,*], Nonhlangabezo Mabuba [d], Damian C. Onwudiwe [a,b], Seshibe Makgato [c]

[a] Department of Chemistry, School of Physical and Chemical Sciences, Faculty of Natural and Agricultural Sciences, North-West University, Mafikeng Campus, Private Bag X2046, Mmabatho 2735, South Africa
[b] Material Science Innovation and Modelling (MaSIM) Research Focus Area, Faculty of Natural and Agricultural Sciences, North-West University, Mafikeng Campus, Private Bag X2046, Mmabatho 2735, South Africa
[c] Department of Chemical Engineering, College of Science, Engineering and Technology, University of South Africa, Florida Campus, 1710 Johannesburg, South Africa
[d] Department of Chemical Sciences, University of Johannesburg, Doornfontein 2028, South Africa

ARTICLE INFO

Keywords:
Photooxidation
Photoreduction
p-n heterojunction
Pharmaceutical mineralization
Cr (VI) photoreduction
Electron redistribution

ABSTRACT

We report the successful design of a heterojunction comprising p-type $CuBi_2O_4$ (CBO) and n-type MoS_2 semiconductors. This was achieved through a hydrothermal and calcination method, resulting in the uniform deposition of three-dimensional CBO nano-cubes onto the surface of two-dimensional MoS_2 nanosheets. Under visible light, the best MoS_2/CBO composite exhibited the maximum catalytic efficacy for both the reduction of Cr (VI) and the oxidation of tetracycline hydrochloride (TC) at a molar ratio of 10:1. For tetracycline degradation the heterostructure achieved 83 % efficiency and a rate constant of 0.00412 min^{-1} after 180 min, while complete reduction of Cr(VI) was achieved, with a rate constant of 0.11 min^{-1} after 40 min. The efficiency of MoS_2/CBO was averagely 1.4 times higher than that of the pristine materials for TCE degradation, while the activity was almost 1.8 times of the pristine materials for Cr(VI) reduction. The remarkable catalytic activity can be ascribed to the combined effects of electron redistribution and charge transfer between 2D MoS_2 and 3D $CuBi_2O_4$ leading to the formation of a heterostructure and thereby facilitating strong interfacial interactions among the components causing effective absorption of visible light and improved separation of photogenerated electron-hole pairs. It is important to note that MoS_2/CBO demonstrated excellent stability and reusability after 6 cycles. The primary reactive species responsible for TC degradation were identified as photo-generated h^+, and $^{\bullet}O^{2-}$. Additionally, e^- was found to be mainly liable for Cr (VI) photoreduction. Furthermore, we propose a plausible photocatalytic reaction pathway for the elimination of both TC and Cr(VI). This research provides valuable inroads into the development of heterojunction photocatalysts for efficient water de-toxification.

1. Introduction

The occurrence of pharmaceuticals and heavy metals in both industrial effluents and natural water supplies is a significant environmental and health challenge owing to their harmful nature to humans and non-biodegradability [1–3]. Tetracycline is one of the most widely used antibiotics due to its effectiveness and affordability [4–6]. However, its high solubility in water and low metabolism signifies its potential for long-term accumulation in the human body and the environment, which is a great risk to human health [7–11]. Consequently, the development of new wastewater treatment technologies has therefore garnered much attention in recent decades [12–14].

Advanced oxidation processes (AOPs) such as persulfate activation, Fenton process, ozonation, and photocatalysis are identified as effective techniques for recalcitrant pollutant removal [15–17]. Semiconductor-based heterogeneous photocatalytic processes offer a potentially cost-effective, simple, and effective technique for pollutant removal from water. Several techniques such as doping, surface modification, and heterostructure formation have been identified for enhancing photocatalytic performance [18]. The formation of heterojunctions is

* Corresponding author.
E-mail address: yusuftl@unisa.ac.za (T.L. Yusuf).

https://doi.org/10.1016/j.jwpe.2024.105074
Received 9 January 2024; Received in revised form 21 February 2024; Accepted 25 February 2024
Available online 1 March 2024

considered the most effective, with an increasing understanding of the nature of charge transfer at the interface of the materials [19–21]. Heterostructure semiconductors often benefit from an improvement in their light response range due to the difference in band gap energy. Furthermore, the lattice match at the junction area of the heterostructure plays a vital role in improving the charge carrier separation as a mismatch may lead to defect formation, which traps charge carriers [22]. In p-n heterojunction, three charge transfer mechanisms have been identified: type II, Z-scheme, and S-scheme. While the type II and S-scheme mechanisms require the establishment of direct electrical contact between the semiconductors, the Z-scheme relies on the formation of ohmic contact at the interface of the semiconductors [23,24].

Dichalcogenides and ternary metal oxides of transition metals such as $CuFe_2O_4$, $CuBi_2O_4$, WS_2, WSe_2 and MoS_2 are well-explored catalytic materials for pollutant degradation. Recently, ternary metal oxides have gained much attention due to their stoichiometry dependent electronic and optical properties that can be easily tuned for improved activity. $CuBi_2O_4$ is a p-type semiconductor with a band gap energy of 1.5–1.7 eV, which makes it a suitable photocatalytic material [25]. Owing to its narrow bandgap, $CuBi_2O_4$ displays a strong visible light absorption, however, it suffers from fast charge recombination and low absorptivity [26]. The compositing of $CuBi_2O_4$ with other semiconductors into a p-n heterojunction can enhance visible light response and stability, while mitigating the high charge carrier recombination experienced by both materials. For example, p-n heterojunctions such as $CuBi_2O_4/TiO_2$ [27], $Bi_2MoO_6/CuBi_2O_4$ [28], $CoFe_2O_4/CuBi_2O_4$ [29], and $CuBi_2O_4/BiVO_4$ [30] have been reported with enhanced photocatalytic activities.

MoS_2 is a two-dimensional (2D) semiconductor with excellent optical and electronic properties and stability. It also possess a strong visible light absorption capacity because of its narrow band of ~1.7 eV [31]. MoS_2 is suitable for the formation of heterostructure because of its layered structure and its properties can be effectively modulated by varying the layer thickness [32]. Forming a MoS_2 heterostructure with $CuBi_2O_4$ as a cocatalyst will lead to a p-n heterojunction, which could significantly enhance charge carrier separation and improve the photocatalytic efficiency of the material. In this study, pristine CBO and MoS_2 were obtained through hydrothermal processes, while the MoS_2/CBO composites were prepared through a facile calcination technique. The CBO was used as a co-catalyst to form the p-n heterojunction for enhancing the photocatalytic activity toward pollutant degradation. The MoS_2/CBO showed improved charge separation, which significantly enhanced the photoreduction and photooxidation of Cr (VI) and tetracycline, respectively.

2. Methodology

2.1. Materials

All reagents were purchased from Sigma-Aldrich (South Africa). Copper nitrate hemihydrate ($Cu(NO_3).3H_2O$, bismuth nitrate pentahydrate ($Bi(NO_3)_3.5H_2O$), ammonium heptamolybdate tetrahydrate ($(NH_4)_6Mo_7O_{24}.4H_2O$), thioacetamide (C_2H_5NS), tetracycline hydrochloride (TC), silver nitrate ($AgNO_3$), polyvinylidene fluoride (PVDF), *N*-methyl-2-pyrrolidone (NMP), Ethylenediaminetetraacetic acid disodium salt dihydrate (Na_2EDTA), tert-butanol (t-BuOH), acrylamide, potassium chromate ($K_2Cr_2O_7$), potassium hexacyanoferrate (II) ($K_4Fe(CN)_6$) and potassium hexacyanoferrate (III) ($K_3Fe(CN)_6$) were used without further purification.

2.2. Synthesis of MoS_2

MoS_2 was synthesized using hydrothermal methods. Simply, an equal amount of ammonium heptamolybdate tetrahydrate and thioacetamide were weighed into a beaker containing 50 mL deionized water. The homogeneous mixture was stirred for 30 min and thereafter was transferred into a Teflon-lined stainless-steel autoclave. The autoclave was heated in a muffle furnace at 180 °C for 6 h and the resulting black powder was washed with H_2O and ethanol and allowed to dry at 110 °C for 4 h.

2.3. Synthesis of $CuBi_2O_4$

$CuBi_2O_4$ was synthesized using hydrothermal methods. Firstly, 0.348 g $Cu(NO_3)_2.3H_2O$, 1.358 g of $Bi(NO_3)_3.5H_2O$, and 1.68 g NaOH were mixed in 50 mL of water with continuous stirring for 1 h. The solution was transferred into a 100 mL autoclave and heated at 180 °C for 6 h in a furnace. The dark brown CBO powder obtained was recovered by centrifugation and dried in a vacuum.

2.4. Synthesis of MoS_2/CBO

A straightforward calcination method was employed in the preparation of MoS_2/CBO. In brief, 1 mg of MoS_2 was measured and placed in a mortar. CBO, in weight ratios of 10 %, 20 %, and 50 %, was then added and thoroughly ground with the MoS_2. Subsequently, the well-mixed blend was transferred into a crucible and heated at 300 °C for a duration of 2 h and cooled down to room temperature. These materials, with weight ratios of 10 wt%, 20 wt%, and 50 wt%, were designated as MoS_2/CBO10, MoS_2/CBO20, and MoS_2/CBO50, respectively.

2.5. Characterization

The X-ray crystallographic data were obtained from d8 Advanced XRD diffractometer with Cu Kα radiation (λ = 154.18 pm). For morphological properties scanning electron microscopy (SEM) and transmission electron microscopy (TEM) recorded on TECNAI G2 (ACI) equipment (Hillsboro, OR, USA) operating with an accelerating voltage of 200 kV were used. A spectroquant® 300 spectrophotometer was used in recording the Fourier transformed infrared (FTIR) spectra. The UV–vis data was acquired on a Cary 60 UV–vis spectrometer (Agilent Technologies, Malaysia). X–ray photoelectron spectroscopy (XPS) data were obtained on Kratos Axis supra+; fitted with monochromatic Al Ka (hv = 1486.6 eV) operating at 150 W. The Autolab Potentiostat workstation (PGSTAT204, Netherlands) was employed to acquire data for electrochemical impedance spectroscopy and Mott-Schottky analysis. The experimental setup consisted of a three-electrode configuration: using platinum sheet as a counter electrode, an Ag/AgCl electrode (3.0 M KCl) as the reference electrode, and a working electrode. To prepare the working electrode, a fluorine-doped tin oxide (FTO) substrate, with a geometric area of 1.5 cm by 1.5 cm was coated with 30 mg of the synthesized material using 5 wt% PVDF, and 100 μL NMP as binder. For the impedance spectroscopic investigation, a solution comprising 5 mM $[Fe(CN)_6]^{3-}/[Fe(CN)_6]^{4-}$ in a 0.1 M KCl medium was prepared. The collected impedance data was analyzed using a Randle circuit model. Mott-Schottky measurements were conducted under dark conditions using a 5 mM $[Fe(CN)_6]^{3-}/[Fe(CN)_6]^{4-}$ solution in a 0.1 M KCl electrolyte. The photocurrent density was obtained in 0.1 M Na_2SO_4, with an applied bias potential of 1.5 V relative to the Ag/AgCl reference electrode. The extent of total organic carbon (TOC) removal (%) was determined by using a Teledyne Tekmar TOC fusion instrument to validate the level of TC molecule mineralization. The photoluminescence spectra were recorded on Shimadzu spectro fluorophotometer RF-6000.

2.6. Photocatalytic Cr(VI) reduction and tetracycline oxidation evaluation

A 100 W Xenon lamp was used as a light source for Tetracycline oxidation and Chromium (VI) reduction. The lamp was located 10 cm from the solution level to investigate the photooxidation of TC (5 mgL^{-1}, 50 mL) and photoreduction of Cr(VI) (5 mgL^{-1}, 50 mL). The pollutant solution was stirred with 30 mg of the catalyst in dark conditions for 30

min to achieve equilibrium. Subsequently, the sample was illuminated, and a 3 mL aliquot of the pollutant was drawn from the bulk solution and centrifuged for 10 min with 7000 rpm to efficiently separate the catalyst. The supernatant liquid was analyzed on a UV–Visible spectrophotometer at a wavelength of 357 nm. The concentration of Cr(VI) was determined by 1, 5-diphenylcarbazide (DPC) method [33].

The below formula was utilized to assess the photocatalytic degradation efficiency:

$$\%Degradation = \left(1 - \frac{C_t}{C_0}\right) \times 100\% \quad (1)$$

In this equation, C_0 (mg/L) represents the initial concentration of TC/Cr(VI), while C_t (mg/L) represents the concentration of the analyte, at time t.

The recyclability of the catalyst was studied by washing the catalyst thrice with water and ethanol and drying it at 80 °C for 5 h before it was reused for the next experiment. The photoreduction and photooxidation experiments were done in triplicates.

The primary reactive species were investigated by performing scavenger experiments with the presence of various scavengers, such as acrylamide, tert-butanol(t-BuOH), EDTA (0.2 mmol/L), or $AgNO_3$ (0.2 mmol/L) to scavenge superoxide, hydroxyl radial, holes and electrons, respectively.

3. Result and discussions

3.1. Structure and morphology

The pristine MoS_2 and CBO were synthesized by facile hydrothermal method while MoS_2/CBO was fabricated by calcination method. The

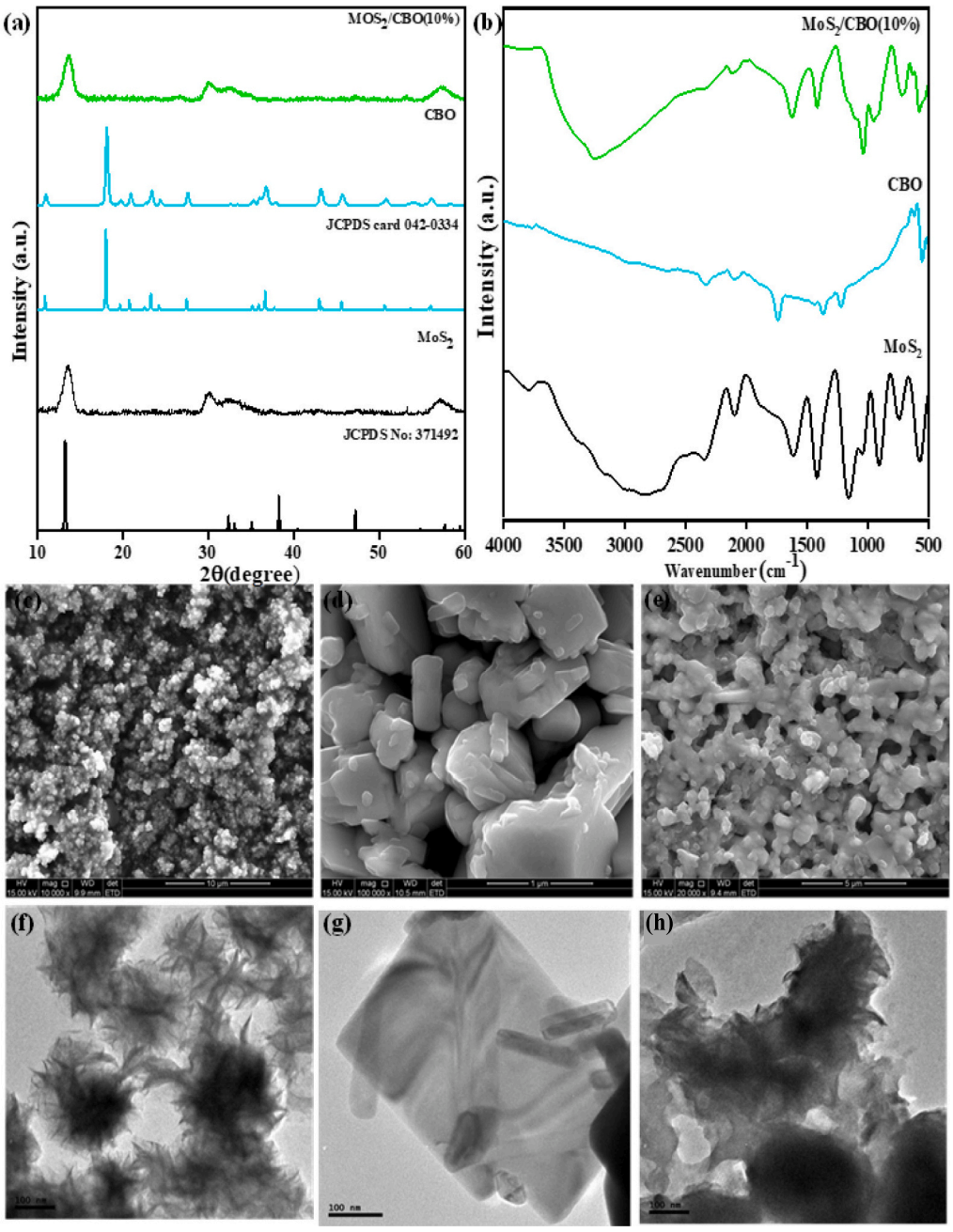

Fig. 1. (a) XRD patterns of MoS_2, CBO and MoS_2/CBO10, (b) FTIR spectra of MoS_2, CBO and MoS_2/CBO10; (c-e) SEM micrographs of MoS_2, CBO and MoS_2/CBO10 and (f-h) SEM images of MoS_2, CBO and MoS_2/CBO10.

structures of MoS_2, CBO and MoS_2/CBO10 composite were assessed using X-ray diffraction (Fig. 1a) The pattern of MoS_2 showed peaks at 32.5° and 57.6° which were characteristic of hexagonal MoS_2, belonging to the *P63/mmc* space group (No.194) [34]. The sharp, broad peak at 2θ = 17° corresponds to the formation of highly crystalline and adjacent few-layered MoS_2 sheets [35]. The pattern of CBO shows peaks at 2θ of 20.8°, 27.9°, 29.8°, 30.9°, 33.2°, 34.4°, 37.6°, 45.0°, 46.8°, 53.10°, 55.6°, 64.8°, 66.0° which was indexed to the tetragonal phase of $CuBi_2O_4$ (JCPDS No. 84–1969). The high intensity of the peaks indicates the high purity and crystallinity of the obtained CBO [36]. The XRD spectra of MoS_2/CBO heterostructure predominately showed peaks due to MoS_2 because of the low content of CBO.

FTIR spectroscopy was used to investigate the materials' surface chemistry (Fig. 1b). The MoS_2 spectra showed broad S—S bond peaks at 564.3 and 898.9 cm^{-1}. A characteristic broad O—H peak, which could be attributed to trapped H_2O was observed at ~3000 cm^{-1}. In the spectra for CBO, the peaks at 540 cm^{-1} and 1211 cm^{-1} are assigned to the Cu—O vibration frequency, and the band at 1361 cm^{-1} are assigned to Bi—O bond [37,38]. The band at 1741 cm^{-1} correlates with the bending vibrations of H_2O [39]. The spectra of MoS_2/CBO10 composites showed a similar pattern to that of MoS_2. The shift in the broad peak at 3000 cm^{-1}, showed that trapped H_2O molecules on MoS_2 is vital in the interaction with CBO. The shift in the O—H was more pronounced in MoS_2/CBO10 confirming the observation from the XRD pattern that there was a stronger interaction between the materials at the lower concentration. The O—H vibrational frequency shift at 1144 cm^{-1} confirms this observation. The FTIR spectra of the composite, therefore, confirm the successful fabrication of MoS_2/CBO heterostructures.

A typical SEM and TEM micrographs of photocatalysts are presented in Fig. 1(c-h). The SEM images showed aggregated MoS_2 were obtained through the hydrothermal process, while CBO, showed a 3-dimensional cube shape. The 3D structures were probably formed by the agglomeration of flat-shaped CBO structures. The SEM image of MoS_2/CBO10 shows the presence of both aggregated sheet like MoS_2 and the 3D CBO structure, confirming the formation of MoS_2/CBO heterostructure. The TEM image of the MoS_2 show the presence of exfoliated nanosheets, while the 3D shape of CBO was more visible in the CBO TEM image. The morphology of MoS_2/CBO10 shown in Fig. 2d indicated that the layered MoS_2 was wrapped around the CBO crystal. The presence of some surface attached CBO was also observed. The TEM micrographs of MoS_2/CBO10 provide more evidence of the heterostructure formation.

The chemical states of the elements in the MoS_2, CBO, and MoS_2/CBO10 were investigated using XPS analysis. Fig. 2a shows the XPS survey scan spectra which verifies the presence of copper, bismuth, oxygen, molybdenum, and sulfur in the pristine and composite semiconductors, thereby confirming the formation of heterojunction. Fig. 2 (b-f) shows the high-resolution XPS spectra of O 1s, Bi 4f, Cu 2p, Mo 3d, and S 2p. In the spectra of O 1s (Fig. 2b), the binding energy of 529.71 eV in the CBO may be ascribed to the lattice oxygen (Cu—O) [40]. However, in MoS_2/CBO10, there was a shift to a higher energy of 531.1 eV indicating chemically bounded oxygen [41]. In the Bi 4f (Fig. 2c) spectra of CBO, the binding energies of 158.0 eV and 163.9 eV which may be assigned to Bi $4f_{7/2}$ and Bi $4f_{5/2}$ shows that the bismuth species was in the +3 oxidation state [42], and were observed to shift to a higher binding energies of 160.6 and 165.9 eV respectively in the Bi 4f spectra of MoS_2/CBO10 (Fig. 2c). In the spectra of Cu 2p of CBO, the oxidation state of Cu was confirmed to be in the +2 state as a result of the distance between the Cu $2p_{3/2}$ and Cu $2p_{1/2}$ peaks observed at 934.1 eV and 954.0 eV respectively, in addition the 2p peaks were accompanied by satellite features [43]. These binding energies were observed to shift to

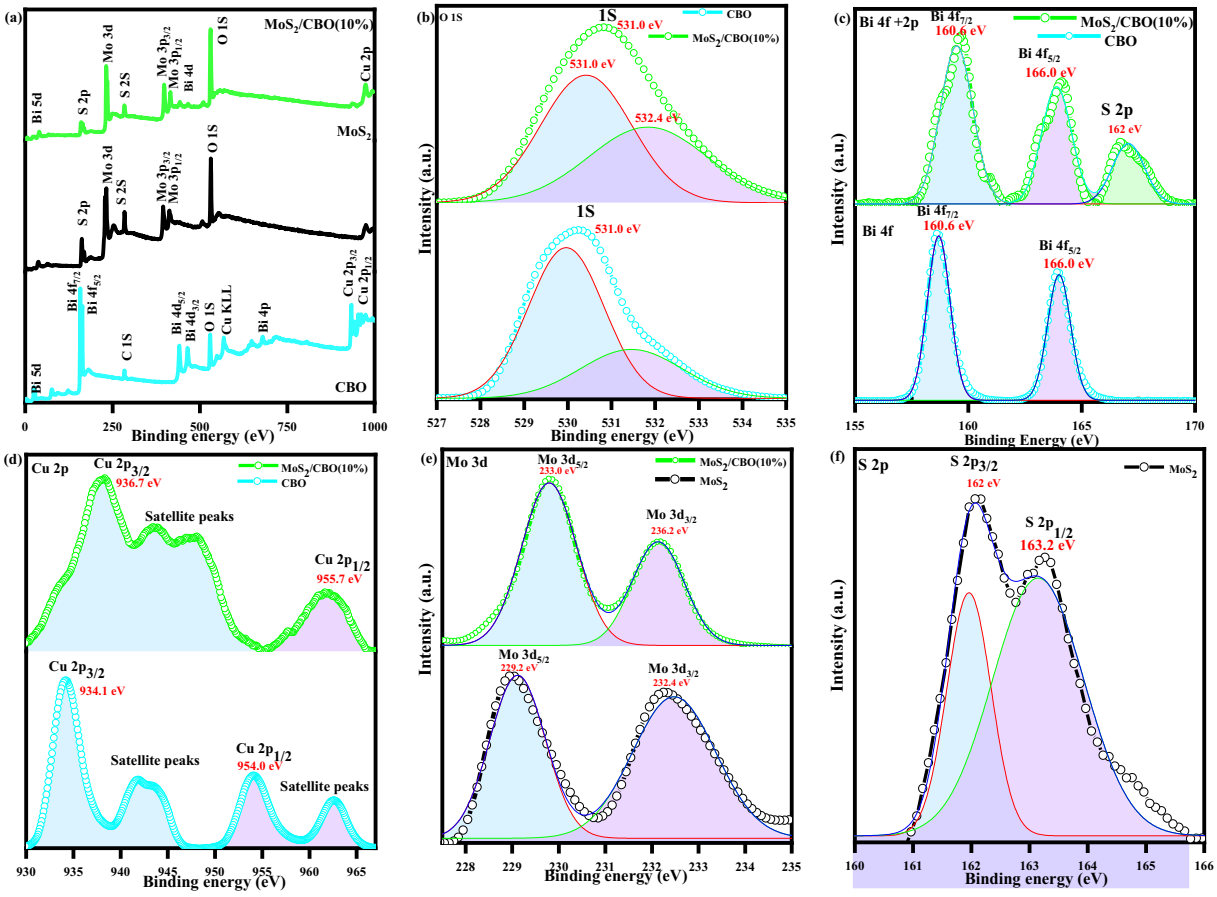

Fig. 2. (a) XPS survey spectra (b) Mo 3d (b) Bi 4f, (c) S 1s (d) Cu 2p and (f) S 2p high resolution scan of MoS_2, CBO10 and MoS_2/CBO10.

higher binding energies of 936.6 eV and 956.7 eV in the spectra of MoS_2/CBO10 (Fig. 2d). In the Mo 3d spectra as shown in Fig. 2e, for MoS_2, the peaks at 229.2 eV and 232.4 eV corresponds to binding energy of $Mo3d_{5/2}$ and Mo $3d_{3/2}$ respectively, which were also observed to shift to a higher energy of 233.1 eV and 232.6 eV in the spectra of MoS_2/CBO10 respectively. The S 2p spectra of MoS_2 has two binding energy peaks at 162.1 eV and 163.2 eV assigned to S $2p_{3/2}$ and S $2p_{1/2}$ respectively [44], whereas in the spectra of MoS_2/CBO, the binding energy of 162.1 eV was observed (Fig. 2f). This peak is associated with sulfide compounds [45]. Basically, the shifts observed in the binding energies of MoS_2 and CBO semiconductors to a higher binding energy to form MoS_2/CBO heterojunction explains that there was redistribution of electrons in the interface of the pristine semiconductors to form the MoS_2/CBO heterojunction [46].

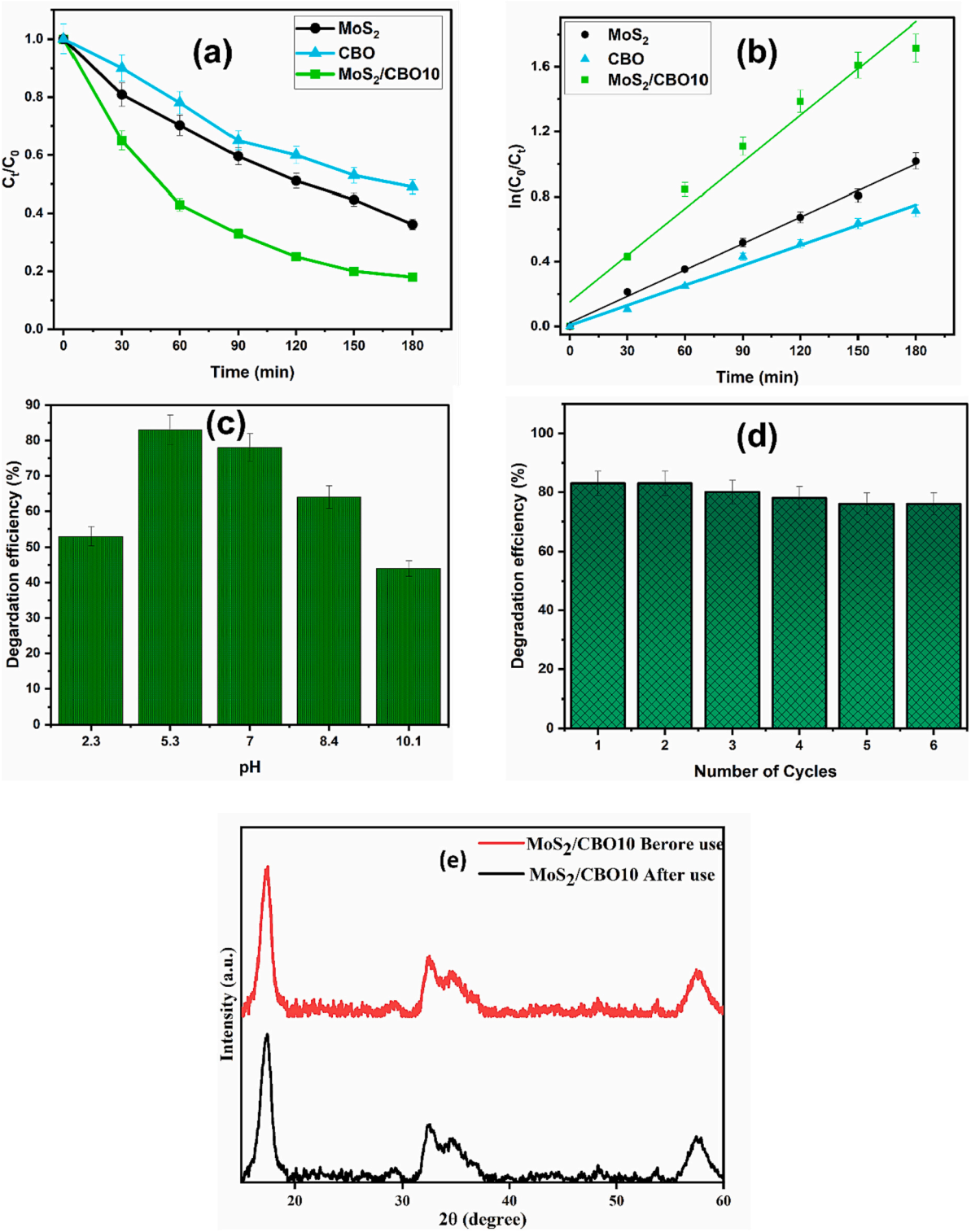

Fig. 3. Photocatalytic degradation of tetracycline (b) kinetics plot of MoS_2 and CBO10, MoS_2/CBO10 (c) effect pH and (d) reusability cycle for the degradation of TC by MoS_2/CBO10 (e) XRD spectra of MoS_2/CBO10 heterojunction before and after photocatalytic activity.

3.2. Photocatalytic degradation studies

3.2.1. Photooxidation of tetracycline

The degradation capability of MoS_2, CBO, and MoS_2/CBO10 heterojunction was evaluated through a light-driven degradation of tetracycline. Tetracycline (TC), is a commonly found clinical antibiotic frequently present in different aqueous environmental sources. The pilot experiment demonstrated the strong stability of TC under visible light. However, these newly fabricated MoS_2/CBO10 heterojunctions exhibited significantly improved photo-oxidation performance against TC (83 %) when compared to pristine MoS_2 (64.5 %), CBO (52.7 %). This indicates that the deliberate construction of a p-n MoS_2/CBO heterojunction plays a vital role in boosting the catalytic efficacy. The TC samples underwent a 180-minute exposure to light without a catalyst present. No alterations in the analyte concentration occurred during this period, indicating the stability of TC in light.

Additionally, the photo-degradation kinetics were determined using pseudo-first-order kinetics:

$$ln\left(\frac{C_t}{C_0}\right) = kt \quad (2)$$

where 'k' = rate constant, and 'C_t' and 'C_0' denote the TC concentration at times 't' and '0', respectively. As shown in Fig. 3b, the obtained 'k' values follow this order: MoS_2/CBO10 > MoS_2 > CBO. Notably, the photoactivity of MoS_2/CBO10 either surpasses or is on par with numerous MoS_2-based heterojunction photocatalysts (Table 1).

The influence of pH on TC degradation using MoS_2/CBO10 was investigated across a wide pH range (2.3, 5.3, 7.0, 8.4, and 10.1) as depicted in Fig. 3c. It is evident that pH significantly affects the degradation of TC by MoS_2/CBO10. Specifically, MoS_2/CBO10 displays its highest activity (83 %) at pH 5.3. Extreme acidic conditions (pH 2.3) or highly alkaline conditions (pH 8.4 or 10.1) are not favorable to TC degradation. This observation is likely attributed to changes in the surface charge of both the catalyst and analyte as pH levels vary [52].

The level of organic compound mineralization is another vital parameter when evaluating the photocatalytic efficacy of a material. We measured the mineralization capacity of MoS_2/CBO10 using TOC measurements. The TOC removal efficiency of around 49 % was achieved after 120 min of exposure to visible light. This outcome underscores the favorable capability of MoS_2/CBO10 in breaking down organic compounds, underscoring its significant potential for wastewater treatment.

To assess the durability of MoS_2/CBO10, we conducted multiple cycles of TC degradation. Notably, there was no substantial decrease in the photocatalytic performance of MoS_2/CBO10 even after subjecting it to six consecutive runs (Fig. 3d). Also, the XRD analysis was conducted again (Fig. 3e) following the degradation of TC. No discernible changes were observed in the spectra of the catalyst, both before and after its use, affirming the stability of the catalyst.

3.2.2. Photoreduction of Cr(VI)

In addition to its effectiveness in photocatalytic oxidation of pharmaceutical antibiotics, MoS_2/CBO10 demonstrates the ability to effectively photocatalyzed the reduction of Cr(VI). We conducted further assessments to evaluate the visible-light photoreduction capacity of MoS_2/CBO10 for Cr(VI) reduction (Fig. 4a). Remarkably, MoS_2/CBO10 achieved the highest efficiency in Cr(VI) reduction, reaching nearly 100 % within just 40 min, surpassing the performance of MoS_2(76 %), CBO (45 %). The enhanced Cr(VI) reduction ability of MoS_2/CBO10 supports the proposed mechanism as discussed later in the manuscript. This is due to the preservation of the photogenerated electrons on CBO, which has a high redox potential and can effectively enable the reduction of Cr(VI) to Cr(III) [53].

Furthermore, MoS_2/CBO10 demonstrated an excellent Cr(VI) reduction rate constant (k) of about 1.1×10^{-1} min^{-1}. The pseudo first kinetics fit of Cr(VI) degradation (Fig. 5c), showed the reaction rate constant for CBO, MoS_2 and MoS_2/CBO was 1.7×10^{-2}, 1.4×10^{-2} and 1.1×10^{-1} min^{-1} (Fig. 4b). These results provide clear evidence that the developed MoS_2/CBO10 exhibits a significantly enhanced photoreduction capability, which can be ascribed to the creation of a p-n heterojunction. In this context, MoS_2/CBO10 holds exceptional promise for catalytic applications in Cr(VI) photo-reduction. The results obtained are comparable to previously reported MoS_2-based photocatalyst (Table 2). The Cr(VI) analyte was also exposed to light without a catalyst. There were no changes in the concentration of the analyte during this period, suggesting the stability of Cr(VI) in light.

To examine the influence of pH on Cr(VI) photoreduction, the degradation was repeated under varying pH spanning from acidic to basic (Fig. 4c). Notably, Cr(VI) reduction shows a gradual improvement as the pH decreases, corroborating well with previously reported observations [59–61]. The optimum photoreduction was achieved at pH = 2.6. In acidic conditions, there is an increased availability of H^+ ions for the efficient reduction of Cr(VI) to Cr(III) (as described in Eqs. (3) and (4)). Conversely, in alkaline conditions, the reduction product formed ($Cr(OH)_3$) from CrO_4^{2-} tends to form precipitates (as per Eq. (5)) that deposit onto MoS_2/CBO10, hindering the reduction of Cr(VI).

$$Cr_2O_7^{2-} + 14H^+ + 6e^- \rightarrow 2Cr^{3+} + 7H_2O \quad (3)$$

$$HCrO_4^- + 7H^+ + 3e^- \rightarrow Cr^{3+} + 4H_2O \quad (4)$$

$$CrO_4^{2-} + 4H_2O + 3e^- \rightarrow Cr(OH)_3 + 5OH^- \quad (5)$$

We studied the effect of catalyst dosage with varying amounts of catalyst. The degradation efficiency increased with increasing catalyst amount. This is due to the increase in active sites on the surface of the photocatalyst (Fig. 4d). Intriguingly, in the 30 mg and 50 mg concentrations, the catalyst gave nearly the same efficiency, hence this experiment was conducted with 30 mg of the MoS_2/CBO photocatalyst.

The reusability of a catalyst is very important for cost-effective use and practical application. The stability of the MoS_2/CBO10 was examined over 6 cycles as shown Fig. 4e. The catalyst only showed a slight loss of activity after the 6th cycle, still maintaining ~90 % efficiency for Cr(VI) reduction, providing further confirmation of its remarkable stability.

3.3. Optical properties and band structure

The photocatalytic activity of semiconductor materials is related to their band structure. The optical characteristics of MoS_2, CBO, and MoS_2/CBO10 heterojunctions were examined using UV–vis DRS (Fig. 5a). In comparison to MoS_2, CBO exhibits a greater light absorption

Table 1
Comparison of TC degradation by previously report MoS_2 based heterojunction photocatalyst.

Photocatalysts	Light source	Catalyst dosage	TC	Degradation	Rate constant	Ref
$MoS_2/FeTiO_3$	Visible light	50 mg	100 mL, 20 mg/L	84.7 %	0.021 min^{-1}	[47]
MoS_2/BiOBr	300 W Xe lamp	50 mg	100 mL, 20 mg/L	68 %	0.011 min^{-1}	[48]
$MoS_2/CdFe_2O_4$	500 W Xe Lamp	25 mg	50 mL, 25 mg/L	87 %	0.00113 min^{-1}	[49]
1T/2H-MoS_2/ZIF-8	300 W Xe Lamp	20 mg	50 mL, 20 mg/L	75.6 %	0.0049 min^{-1}	[50]
Ag/MoS_2/rGO	300 W Xe lamp	40 mg	100 mL, 20 mg/L	85.5 %	0.014 min^{-1}	[51]
MoS_2/CBO10	100 W-Xe Lamp	30 mg	50 mL, 5 mg/L	83 %	0.00412 min^{-1}	This work

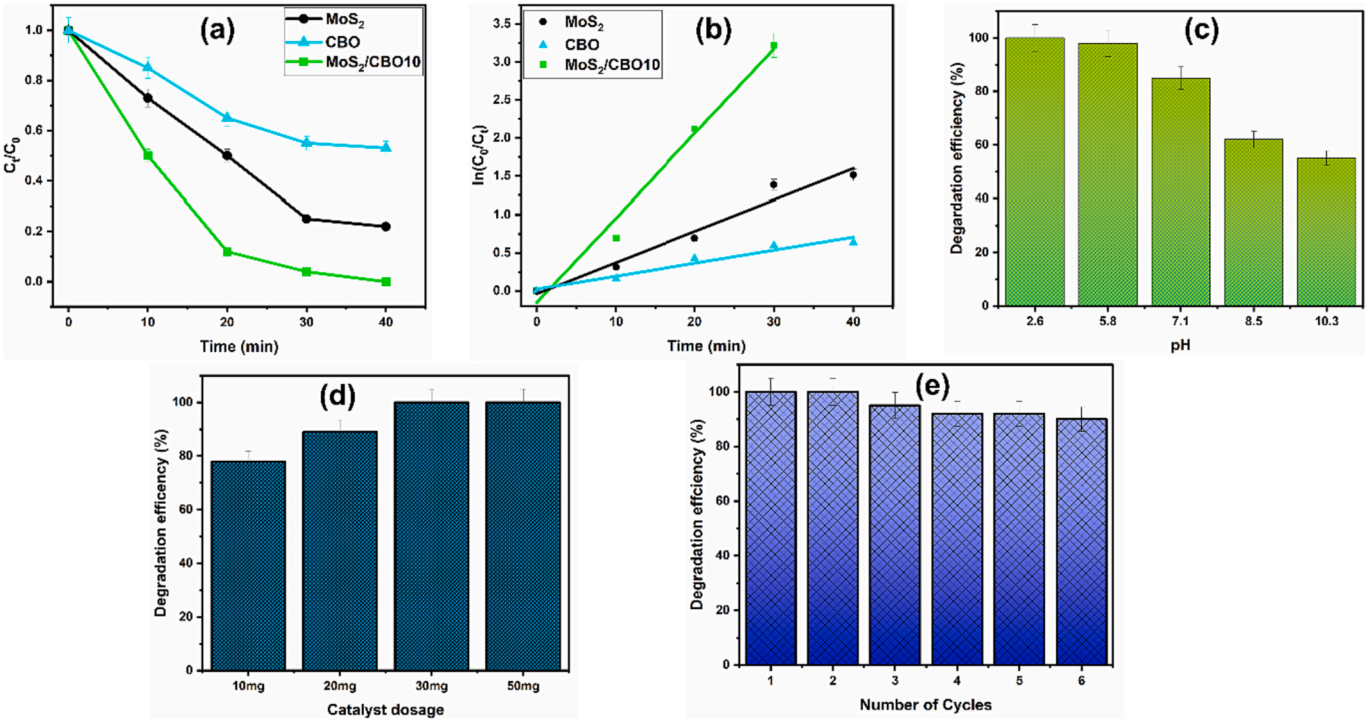

Fig. 4. Photocatalytic reduction of Cr(VI) (b) kinetics plot of MoS_2 and CBO10, MoS_2/CBO10 (c) effect pH and (d) effect of catalyst dosage (e) reusability cycle for the degradation of Cr(VI) by MoS_2/CBO10.

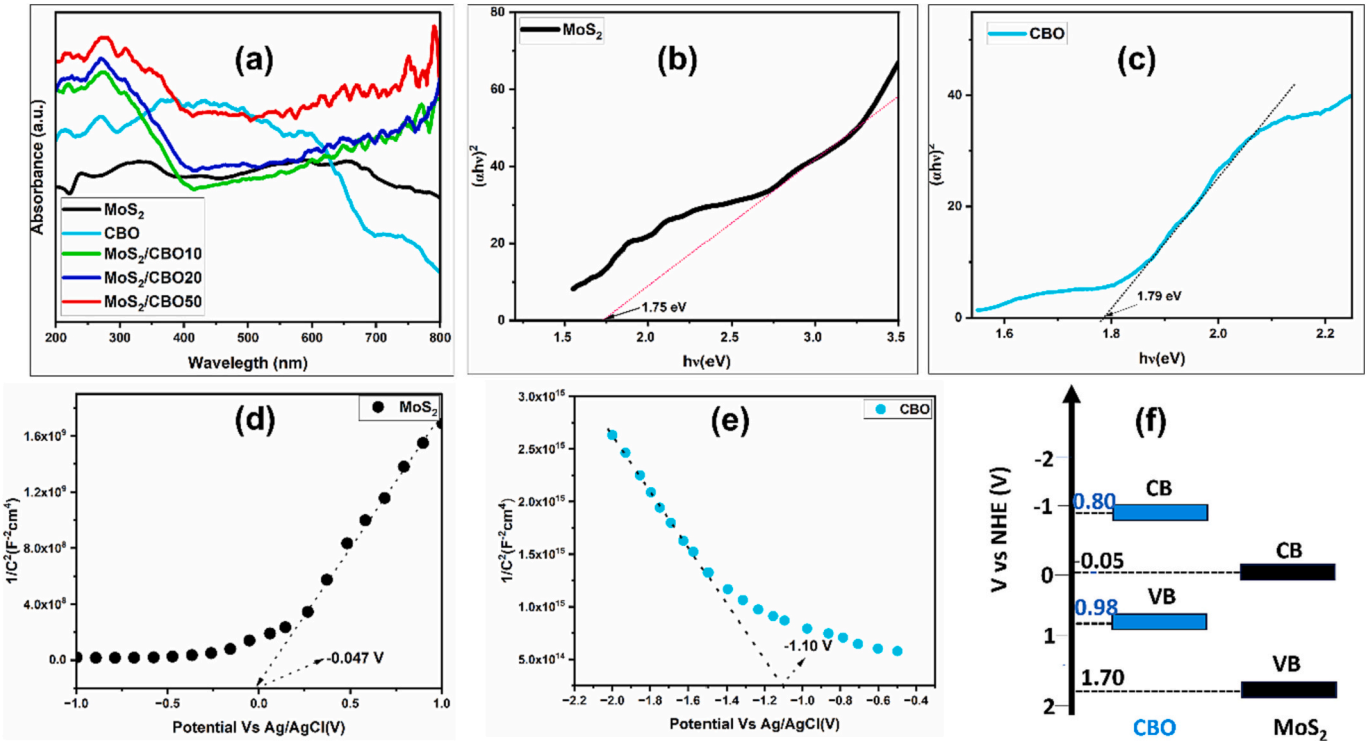

Fig. 5. (a-c) Absorption spectra and Tauc plot of MoS_2, CBO and MoS_2/CBO10 (d-e) Mott-Schottky plot of MoS_2 and CBO and (f) band alignment scheme of MoS_2/CBO10 heterostructure.

profile. Upon heterojunction formation, the resulting MoS_2/CBO10 heterojunctions demonstrate even better light absorption capabilities. Significantly, the MoS_2/CBO10 heterojunctions display an intense absorption band in the visible-light region (450–750 nm). This is credited to the π–π stacking interface and the clustering of MoS_2 [33]. Furthermore, the band gap (E_g) of these catalysts was determined using the Kubelka–Munk equation:

$$ahv = A\,(hv - Eg)^{n/2} \tag{6}$$

The calculated E_g values for MoS_2 and CBO are found to be 1.75 eV

Table 2
Comparison of Cr(VI) degradation by previously report MoS_2 based heterojunction photocatalyst.

Photocatalysts	Light source	Catalyst dosage	Cr(VI)	Degradation	Ref
CeO_2-MoS_2	Xe lamp (300 W)	6 mg	5 mg/L, 20 mL	100 % (120 min)	[54]
MoS_2/SnS_2	Xe lamp (300 W)	10 mg	(120 mg/L 50 mL)	100 % (60 min)	[55]
Ag-MoS_2	Xe lamp (300 W)	20 mg	50 mg/L, 100 mL	100 % (100 min)	[56]
MoS_2/PVP	Xe lamp (300 W)	20 mg	30 mg/L, 50 mL	99 % (180 min)	[57]
RP-MoS2/rGO	Xe lamp (300 W)	20 mg	40 mg/L, 50 mL	98 % (30 min)	[58]
MoS_2/CBO10	Xe lamp (300 W)	30 mg	5 mg/L, 50 mL	100.0 % (40 min)	This Work

and 1.79 eV, respectively.

The band edge position of conduction band (E_{cb}) and valence band (E_{vb}) of MoS_2 and CBO may be evaluated from the below formula:

$$E_{vb} = X - E^e + 0.5E_g \quad (7)$$

$$E_{cb} = E_{vb} - E_g \quad (8)$$

where X = absolute electronegativity of the semiconductor (5.32 and 4.59 eV for MoS_2 and CBO respectively) [62,63], E^e = energy of free electrons on the hydrogen scale (4.5 eV), and E_g is the bandgap energy of the semiconductor.

The absorption spectra of MoS_2, CBO, and MoS_2/CBO10 show an increase in the absorption intensity was observed in the heterostructure compared to the pristine materials. A lowering of band gap energy was also observed from the Tauc plot shown in Fig. 5(b & c). The band gap energy of MoS_2 and CBO estimated from the Tauc plot presented is 1.75 and 1.79 eV. According to Eqs. (7) & (8), the E_{VB} and E_{CB} of MoS_2 are calculated to be 1.70 eV, and −0.05 eV. The E_{VB} and E_{CB} of the CBO are calculated as 0.98 and −0.80 eV, respectively.

Mott-Schottky plots presented in Fig. 5(d&e) for CBO and MoS_2 obtained from ferrocyanide solution were utilized for the determination of flat band potentials and majority carrier densities. The flat band potential was acquired from the extrapolated x-intercept, while the slope provided information about the charge carrier density. The CBO exhibited a negative slope, confirming p-type semiconducting characteristics. While MoS_2 exhibited a positive slope, confirming n-type semiconducting characteristics. The flat band potentials measured for CBO, and MoS_2 were −1.10 and −0.047 V vs Ag/AgCl, respectively. Using the Nernst equation: $E_{NHE} = E_{Ag/AgCl} + 0.197$ (9), the E_{fb} values for MoS_2 and CBO are determined as +0.15 V and −0.90 V vs. NHE, respectively. The flat-band (FB) potentials are typically positioned approximately 0.1 V above the conduction band (CB) potentials in n-type semiconductors. Conversely, in the case of p-type semiconductors, the FB potentials are generally situated approximately 0.1 V below the valence band (VB) potentials [64]. Consequently, the E_{CB} values for MoS_2 and CBO are calculated as −0.05 V and −0.80 V vs. NHE, respectively. Employing the formula: $E_{VB} - E_{CB} = E_g$ (9), the E_{VB} (Valence Band Edge) values for MoS_2 and CBO are confirmed as 1.70 V and 0.98 V vs. NHE, respectively [65]. These data collectively elucidate the band energy structures of MoS_2 and CBO (Fig. 5f.)

The absorption spectra and band alignment of MoS_2/CBO10, shows the broadening of the absorption range of the composite compared to the pristine materials could be a significant factor in the enhanced photocatalytic activity of the heterostructure. The formation of heterostructure substantially extended the absorption edge to longer wavelength and enhances the visible light absorption intensity.

3.4. Photo(electro)chemical properties

To investigate the characteristics of charge transport of the photocatalyst, we conducted measurements using electrochemical impedance spectra (EIS). The semicircular pattern depicted in Fig. 6a is a result of the charge transfer process, with its resistance equating to the semicircle's diameter. Among the materials studied, CBO exhibits notably high charge transfer resistance, surpassing even the pure MoS_2 material with the lowest charge transfer resistance. However, the composites demonstrate lower charge transfer resistance compared to the CBO, which implies that MoS_2 enhanced the ability to facilitate the transfer of photogenerated electrons in the composite. The R_{ct} of the catalysts are in the order CBO > MoS_2/CBO20 > MoS_2/CBO50 > MoS_2/CBO10 > MoS_2. The composite exhibited an enhanced charge separation compared to both pristine materials, as evidenced by the photocurrent response measurements. During irradiation, there is a noticeable spike in the photocurrent, as shown in the photocurrent response (Fig. 6b). This phenomenon can be linked to an increased charging rate, resulting in a surge in capacitance at the interface between the photoanode and the electrolyte. In the dark, a rapid decrease in photo-response is noticed due to the transition of electrons from the semiconductor through substrate and the migration of holes into the electrolyte. Likewise, the decline in photocurrent is ascribed to the recombination of electron-hole pairs within the semiconductor [37,51]. After several cycles of on/off, a state of equilibrium is achieved, signifying a stable state of charge generation and recombination. Notably, the observed photocurrent density in the composite (0.076 $mAcm^{-2}$) is nearly twice as high as that of MoS_2 (0.043 $mAcm^{-2}$) and CBO (0.031 $mAcm^{-2}$).

Recombination of photogenerated charge carriers is a significant factor in the photocatalytic process. From the PL spectra (Fig. 6c.), the pristine CBO displays pronounced photoluminescence emission peaks within the 770–790 nm range. In contrast, there is a notable reduction in the photoluminescence intensity of MoS_2 and all the composites. The heterojunction MoS_2/CBO10 had the least intense emission peak with a 70 % reduction. The lower peak intensity in MoS_2/CBO10 shows lower recombination of the photogenerated charge carriers. Furthermore, the low-energy tailing of the PL suggests the presence of sub-bandgap features caused by defects in the MoS_2/CBO10 heterojunction [66].

The outcomes presented above confirm that MoS_2/CBO10 achieves the most effective separation and transport of spatial electrons and holes. This primarily explains its superior photocatalytic activity.

3.5. Photocatalytic mechanism

From the absorption, PL spectra, and photocurrent response, both MoS_2 and CBO can be simultaneously exited under visible light irradiation to generate electron-hole pairs which were observed to be suppressed in MoS_2/CBO10 heterojunction. As shown in the band alignment schematic in Fig. 5f, MoS_2/CBO10 possesses a staggered band arrangement with the p-n interface, causing a built-in electric field. Fig. 7 shows the radical scavenging experiment for the photocatalytic degradation of TC and Cr(VI). The scavenging experiment for TC (Fig. 7b) shows the significance of the photogenerated holes as the process efficiency was significantly affected by the introduction of EDTA-Na and acrylamide, indicating that holes and superoxide are mostly responsible for TC oxidation. The negligible influence of t-BuOH on the degradation process confirmed the lower redox potential of the available h^+ to initiate the OH^-/•OH radical redox reaction. For Cr(VI) reduction, the scavenging study clearly shows the photogenerated electrons as the major reactive species that facilitated the reduction process.

Based on the bandgap alignment and radical scavenging experiments, a plausible type II charge transfer mechanism was proposed for the MoS_2/CBO heterojunction as shown in Fig. 8. In a type II heterojunction, a built-in field is generated by the spontaneous diffusion of electrons between the two semiconductors as confirmed by XPS analysis.

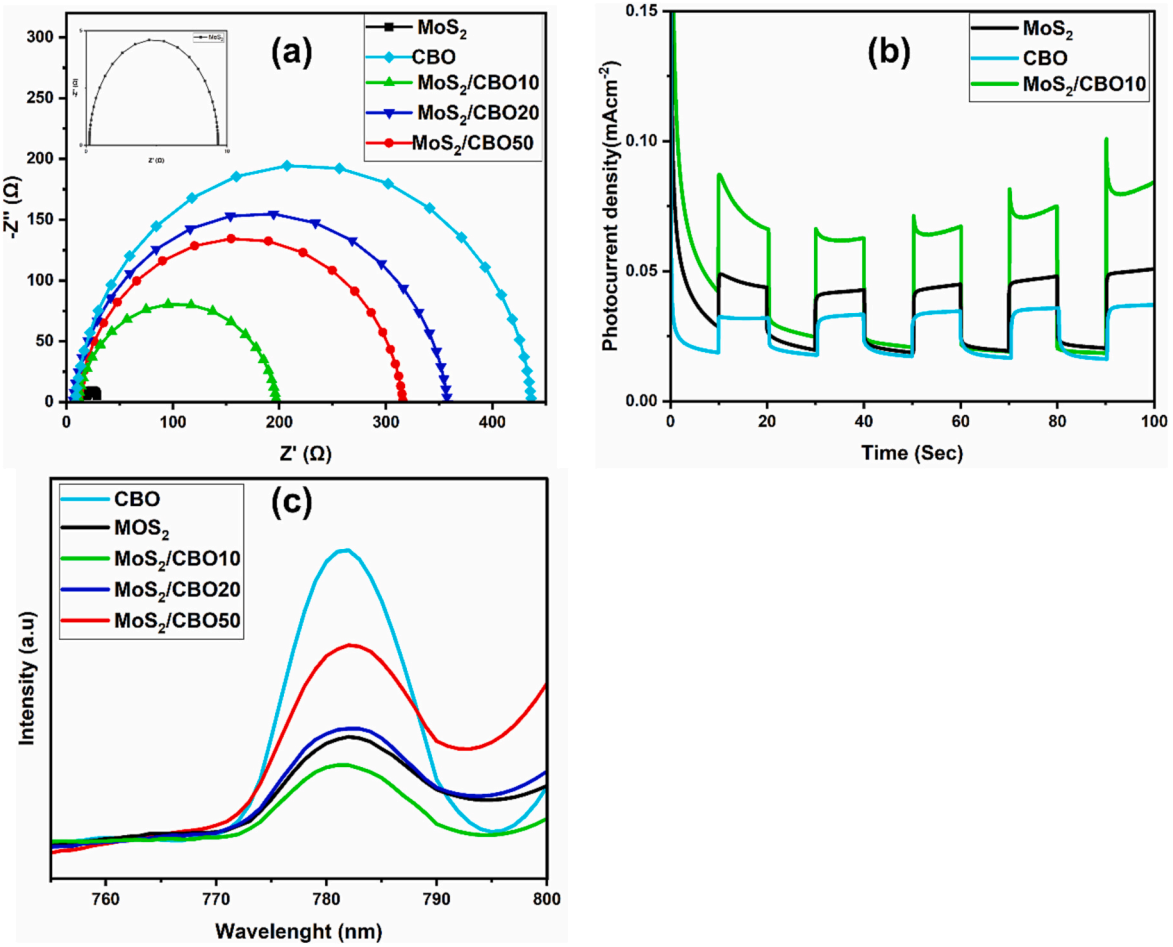

Fig. 6. EIS spectra and (b) photocurrent response (c) PL spectra of the CBO, MoS_2 and MoS2/CBO10.

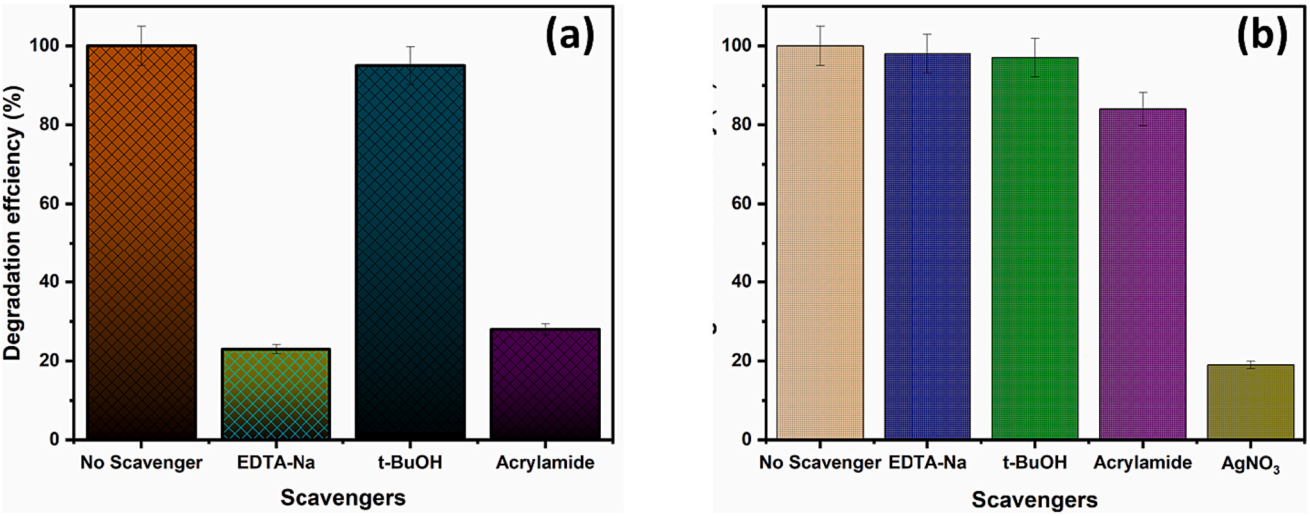

Fig. 7. Radical scavenging for (a) TC and (b) Cr(VI).

There is redistribution of electrons and charge transfer where the electrons from the MoS_2 region move into the CBO region while holes from the CBO region will move to the MoS_2 region, creating a space-charge region on the interface of the MoS_2/CBO heterojunction. These electrons and holes recombine to create a depletion region where the surface of MoS_2 is positively charged, and the surface of CBO becomes negatively charged. This depletion region will then generate the built-in field that will oppose the flow of electrons, thus suppressing the recombination rate. This barrier will help the photogenerated electrons and holes to be long-lived, leading to enhanced charge separation for improved photocatalytic oxidation and reduction. When an electron moves from the CB of MoS_2 to the CB of CBO, it leaves a positive charge behind, while a hole moving from the VB of CBO to the MoS_2 leaves a negative charge. This exchange of electrons and holes continues until the system

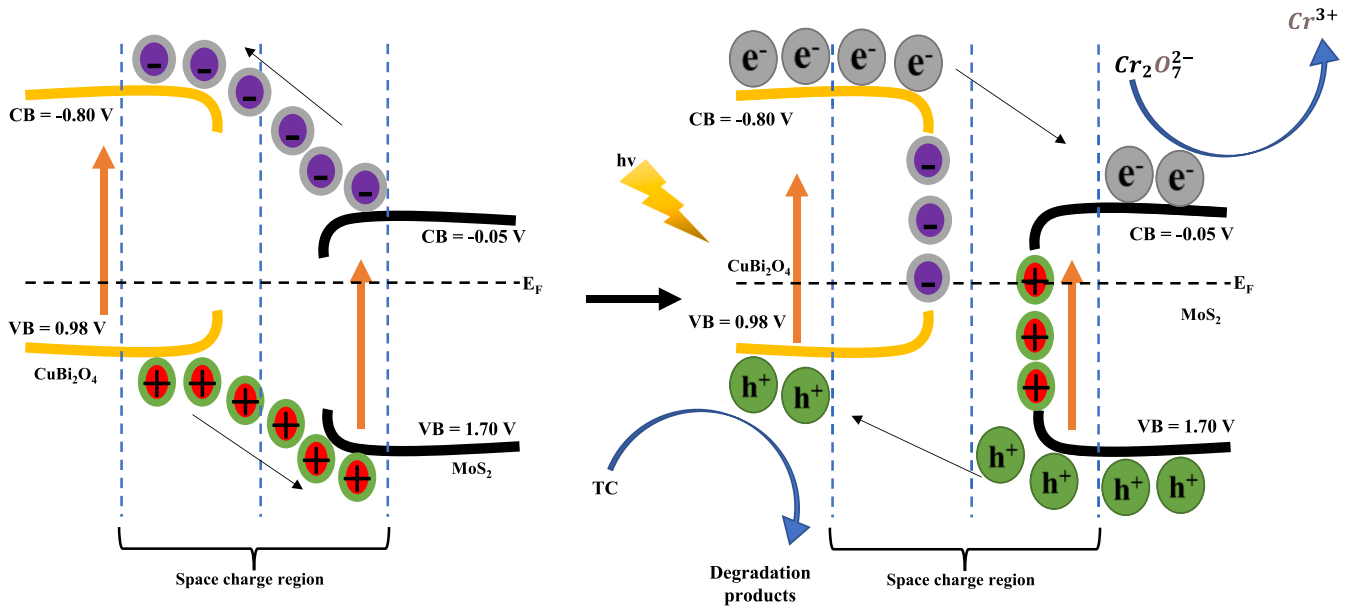

Fig. 8. p-n heterojunction scheme mechanism for the MoS_2/CBO10 heterostructure.
MoS_2/CBO10 + hv → MoS_2/CBO10(e^-, h^+)
h^+(CBO) + e^-(MoS_2) → Recombine.
h^+(MoS_2) + H_2O → X
e^-(CBO) + O_2 → $•O_2^-$
$•O_2^-$(CBO)/ h^+(MoS_2) + TC → CO_2 + H_2O
$•O_2^-$/e^-(CBO) + Cr(VI) → Cr(III).

reaches Fermi-level equilibrium. Consequently, a charged region develops near the p–n interface, known as the internal electric field. Once the internal electric field forms, photoexcited electrons transition from a high conduction band to a low conduction band, and holes move from a low valence band to a high valence band after light excitation. These electron-hole pairs then remain well separated, as depicted in Fig. 8 [67]. The formation of the internal electric field reduces the likelihood of recombination for photoexcited electron-hole pairs, leading to enhanced photocatalytic performance [67].

4. Conclusion

In this study, the successful synthesis of MoS_2/CBO heterostructure through a facile calcination process was presented. The p-n heterostructure, benefited from improved light absorption and enhanced photogenerated charge carrier separation, leading to the enhancement of its photocatalytic activity. Compare to pristine MoS_2 and CBO, MoS_2/CBO showed improved activity for the photocatalytic oxidation and reduction of tetracycline and Cr(VI) respectively. The radical scavenging study revealed that the preservation of charge carriers with high redox potential was significant in enhancing the photocatalytic activity of the catalyst. The stability of the obtained composite was also affirmed with its sustained activity after 6 cycles. The findings in this study can advance the creation of more efficient p-n heterojunction composite photocatalysts to address environmental demands for future progress.

CRediT authorship contribution statement

Olalekan C. Olatunde: Writing – review & editing, Writing – original draft, Methodology, Investigation, Formal analysis, Data curation, Conceptualization. **Tunde L. Yusuf:** Writing – review & editing, Writing – original draft, Supervision, Methodology, Investigation, Formal analysis, Data curation, Conceptualization. **Nonhlangabezo Mabuba:** Resources, Project administration. **Damian C. Onwudiwe:** Writing – review & editing, Writing – original draft, Visualization, Validation, Supervision, Resources, Project administration. **Seshibe Makgato:** Visualization, Validation, Resources, Project administration.

Declaration of competing interest

The authors declare that they have no known competing financial interests or personal relationships that could have appeared to influence the work reported in this paper.

Data availability

Data will be made available on request.

Acknowledgements

The authors are grateful to University of South Africa, University of Johannesburg and North-West University, South Africa.

References

[1] Y. Zhang, et al., Electrocatalytic reduction of chromium by poly(aniline-co-o-aminophenol): an efficient and recyclable way to remove Cr(VI) in wastewater, Appl. Catal. B Environ. 92 (3) (2009) 351–356.
[2] R.K. Ibrahim, et al., Environmental application of nanotechnology: air, soil, and water, Environ. Sci. Pollut. Res. 23 (2016) 13754–13788.
[3] H.K. Okoro, et al., Potentially toxic elements in pharmaceutical industrial effluents: a review on risk assessment, treatment, and management for human health, Sustainability 15 (8) (2023) 6974.
[4] H. Wang, et al., Visible-light-driven removal of tetracycline antibiotics and reclamation of hydrogen energy from natural water matrices and wastewater by polymeric carbon nitride foam, Water Res. 144 (2018) 215–225.
[5] G. Gopal, et al., A review on tetracycline removal from aqueous systems by advanced treatment techniques, RSC Adv. 10 (45) (2020) 27081–27095.
[6] D. Wang, et al., Simultaneously efficient adsorption and photocatalytic degradation of tetracycline by Fe-based MOFs, J. Colloid Interface Sci. 519 (2018) 273–284.
[7] K. Zhu, et al., Encapsulation of Fe0-dominated Fe3O4/Fe0/Fe3C nanoparticles into carbonized polydopamine nanospheres for catalytic degradation of tetracycline via persulfate activation, Chem. Eng. J. 372 (2019) 304–311.
[8] S.M. Zainab, et al., Antibiotics and antibiotic resistant genes (ARGs) in groundwater: a global review on dissemination, sources, interactions, environmental and human health risks, Water Res. 187 (2020) 116455.

[9] D. Pradhan, et al., Recent bioreduction of hexavalent chromium in wastewater treatment: a review, J. Ind. Eng. Chem. 55 (2017) 1–20.
[10] H.-B. Kim, et al., Consecutive reduction of Cr(VI) by Fe(II) formed through photo-reaction of iron-dissolved organic matter originated from biochar, Environ. Pollut. 253 (2019) 231–238.
[11] S. Kalidhasan, et al., The journey traversed in the remediation of hexavalent chromium and the road ahead toward greener alternatives—a perspective, Coord. Chem. Rev. 317 (2016) 157–166.
[12] V. Kumar, S. Dwivedi, A review on accessible techniques for removal of hexavalent chromium and divalent nickel from industrial wastewater: recent research and future outlook, J. Clean. Prod. 295 (2021) 126229.
[13] A. Babuponnusami, et al., Advanced oxidation process (AOP) combined biological process for wastewater treatment: a review on advancements, feasibility and practicability of combined techniques, Environ. Res. 237 (2023) 116944.
[14] E.I. El-Aswar, et al., A comprehensive review on preparation, functionalization and recent applications of nanofiber membranes in wastewater treatment, J. Environ. Manag. 301 (2022) 113908.
[15] T. Mohlala, et al., Photoelectrocatalytic degradation of emerging organic pollutants in water on an FTO/BiVO4/NiS photoanode, J. Electroanal. Chem. 947 (2023) 117806.
[16] T.L. Yusuf, et al., The application of photoelectrocatalysis in the degradation of rhodamine B in aqueous solutions: a review, RSC Adv. 12 (40) (2022) 26176–26191.
[17] D. Masekela, et al., Application of BaTiO3-based catalysts for piezocatalytic, photocatalytic and piezo-photocatalytic degradation of organic pollutants and bacterial disinfection in wastewater: a comprehensive review, Arab. J. Chem. 16 (2022) 104473.
[18] T.L. Yusuf, et al., Photoelectrocatalytic degradation of sulfamethoxazole over S–Scheme Co3Se4/BiVO4 heterojunction photoanode: an experimental and density functional theory investigations, Surf. Interfaces 36 (2023) 102534.
[19] M. Xia, et al., Rational catalyst design for spatial separation of charge carriers in a multi-component photocatalyst for effective hydrogen evolution, J. Mater. Chem. A 10 (48) (2022) 25380–25405.
[20] X. Wang, et al., Fabrication of 0D/1D S-scheme CoO-CuBi2O4 heterojunction for efficient photocatalytic degradation of tetracycline by activating peroxydisulfate and product risk assessment, J. Colloid Interface Sci. 661 (2024) 943–956.
[21] T.L. Yusuf, et al., Theoretical and experimental insight into the construction of FTO/NiSe2/BiVO4 photoanode towards an efficient charge separation for the degradation of pharmaceuticals in water, J. Environ. Chem. Eng. 11 (5) (2023) 110711.
[22] Y. Wang, et al., Visible light driven type II heterostructures and their enhanced photocatalysis properties: a review, Nanoscale 5 (18) (2013) 8326–8339.
[23] Q. Xiang, J. Yu, M. Jaroniec, Graphene-based semiconductor photocatalysts, Chem. Soc. Rev. 41 (2) (2012) 782–796.
[24] S. Bai, et al., Steering charge kinetics in photocatalysis: intersection of materials syntheses, characterization techniques and theoretical simulations, Chem. Soc. Rev. 44 (10) (2015) 2893–2939.
[25] Y. Liu, et al., Fabrication of CuBi2O4/Bi2MoO6 pn heterojunction as synergistic photoelectric catalyst for efficient removal of ciprofloxacin in photo-electro-Fenton-like system, J. Water Process Eng. 52 (2023) 103534.
[26] W.-D. Oh, et al., A novel three-dimensional spherical CuBi2O4 consisting of nanocolumn arrays with persulfate and peroxymonosulfate activation functionalities for 1 H-benzotriazole removal, Nanoscale 7 (17) (2015) 8149–8158.
[27] A.S. Mary, C. Murugan, A. Pandikumar, Uplifting the charge carrier separation and migration in co-doped CuBi₂O₄/TiO₂ p-n heterojunction photocathode for enhanced photoelectrocatalytic water splitting, J. Colloid Interface Sci. 608 (2022) 2482–2492.
[28] Z. Li, et al., In−situ mechanochemical fabrication of p-n Bi₂MoO₆/CuBi₂O₄ heterojunctions with efficient visible light photocatalytic performance, J. Alloys Compd. (2021) 882.
[29] M. Ghobadifard, P.V. Radovanovic, S. Mohebbi, Novel CoFe₂O₄/CuBi₂O₄ heterojunction p-n semiconductor as visible-light-driven nanophotocatalyst for C (OH)-H bond activation, Appl. Organomet. Chem. 36 (4) (2022).
[30] S.P. Liu, et al., Pulsed laser/electrodeposited CuBi₂O₄/BiVO₄ p-n heterojunction for solar water splitting, Sol. Energy Mater. Sol. Cells 180 (2018) 123–129.
[31] F. Guo, et al., Fabrication of p-n CuBi2O4/MoS2 heterojunction with nanosheets-on-microrods structure for enhanced photocatalytic activity towards tetracycline degradation, Appl. Surf. Sci. 491 (2019) 88–94.
[32] R. Yang, J. Fan, M. Sun, Transition metal dichalcogenides (TMDCs) heterostructures: optoelectric properties, Front. Phys. 17 (4) (2022) 43202.
[33] C. Wang, et al., Rationally designed tetra (4-carboxyphenyl) porphyrin/graphene quantum dots/bismuth molybdate Z-scheme heterojunction for tetracycline degradation and Cr(VI) reduction: performance, mechanism, intermediate toxicity appraisement, J. Colloid Interface Sci. 619 (2022) 307–321.
[34] K. Wu, et al., Preparation of hydrophobic MoS2, NiS2-MoS2 and CoS2-MoS2 for catalytic hydrodeoxygenation of lignin-derived phenols, Mol. Catal. 477 (2019) 110537.
[35] X. Wang, et al., Morphology-controlled synthesis of MoS2 nanostructures with different lithium storage properties, J. Alloys Compd. 600 (2014) 84–90.
[36] A. Tikoo, et al., Mechanistic insights into enhanced photocatalytic H2O2 production induced by a Z-scheme heterojunction of copper bismuth oxide and molybdenum sulfide, J. Mater. Chem. A 11 (27) (2023) 14887–14899.
[37] M. Ghobadifard, P.V. Radovanovic, S. Mohebbi, Novel CoFe2O4/CuBi2O4 heterojunction p–n semiconductor as visible-light-driven nanophotocatalyst for C (OH)–H bond activation, Appl. Organomet. Chem. 36 (4) (2022) e6612.
[38] P.J. Mafa, et al., Cobalt oxide/copper bismuth oxide/samarium vanadate (Co3O4/CuBi2O4/SmVO4) dual Z-scheme heterostructured photocatalyst with high charge-transfer efficiency: enhanced carbamazepine degradation under visible light irradiation, J. Colloid Interface Sci. 603 (2021) 666–684.
[39] N.S. Gudipati, et al., Electrochemical detection of 4-nitrophenol on nanostructured CuBi2O4 with plausible mechanism supported by DFT calculations, J. Environ. Chem. Eng. 10 (6) (2022) 108758.
[40] H. Jaim, et al., Stability of the oxygen vacancy induced conductivity in BaSnO 3 thin films on SrTiO 3, Appl. Phys. Lett. 111 (2017) 172102.
[41] T.J. Frankcombe, Y. Liu, Interpretation of oxygen 1s X-ray photoelectron spectroscopy of ZnO, Chem. Mater. 35 (14) (2023) 5468–5474.
[42] Y. Nakabayashi, M. Nishikawa, Y. Nosaka, Fabrication of CuBi2O4 photocathode through novel anodic electrodeposition for solar hydrogen production, Electrochim. Acta 125 (2014) 191–198.
[43] S.P. Berglund, et al., Comprehensive evaluation of CuBi2O4 as a photocathode material for photoelectrochemical water splitting, Chem. Mater. 28 (12) (2016) 4231–4242.
[44] A. Hezam, et al., 2D/1D MoS2/TiO2 heterostructure photocatalyst with a switchable CO2 reduction product, Small Methods 7 (1) (2023) 2201103.
[45] T. Tudino, et al., Influence of dimethylsulfoxide and dioxygen in the fructose conversion to 5-hydroxymethylfurfural mediated by Glycerol's acidic carbon, Front. Chem. 8 (2020) 263.
[46] J. Hu, et al., Improved Interface charge transfer and redistribution in CuO-CoOOH p-n heterojunction nanoarray electrocatalyst for enhanced oxygen evolution reaction, Adv. Sci. 8 (22) (2021) 2103314.
[47] P. Zhu, et al., Construction of 3D flower-like FeTiO3/MoS2 heterostructure photocatalyst for degradation of tetracycline hydrochloride, J. Alloys Compd. 937 (2023) 168425.
[48] W. Yin, et al., In-situ synthesis of MoS2/BiOBr material via mechanical ball milling for boosted photocatalytic degradation pollutants performance, ChemistrySelect 6 (5) (2021) 928–936.
[49] H. Wang, et al., Synthesis of magnetic Z-scheme MoS2/CdFe2O4 composite for visible light induced photocatalytic degradation of tetracycline, Mater. Sci. Semicond. Process. 152 (2022) 107075.
[50] W.-Q. Chen, et al., MoS2/ZIF-8 hybrid materials for environmental catalysis: solar-driven antibiotic-degradation engineering, Engineering 5 (4) (2019) 755–767.
[51] S. Li, et al., Fabricated ag dots/flower-like MoS2/rGO multidimensional photocatalyst for enhanced photocatalytic activity, J. Taiwan Inst. Chem. Eng. 104 (2019) 177–186.
[52] S. Li, et al., Constructing Cd0.5Zn0.5S/Bi2WO6 S-scheme heterojunction for boosted photocatalytic antibiotic oxidation and Cr(VI) reduction, Adv. Powder Mater. 2 (1) (2023) 100073.
[53] G. Aimaiti, et al., Nb2O5/red phosphorus S-scheme heterojunction photocatalyst for removal of organic contaminant and Cr(VI): electrochemical performance and mechanism, Mater. Sci. Semicond. Process. 160 (2023) 107421.
[54] H. Wang, et al., Cerium-doped MoS2 nanostructures: efficient visible photocatalysis for Cr(VI) removal, Sep. Purif. Technol. 170 (2016) 190–198.
[55] T. Qiang, et al., Dual modified MoS2/SnS2 photocatalyst with Z-scheme heterojunction and vacancies defects to achieve a superior performance in Cr (VI) reduction and dyes degradation, J. Clean. Prod. 291 (2021) 125213.
[56] K. Sun, et al., Synergistic effect in the reduction of Cr(VI) with Ag-MoS2 as photocatalyst, Appl. Mater. Today 18 (2020) 100453.
[57] Y. Zhang, et al., Enhanced adsorption and photocatalytic Cr(VI) reduction and sterilization of defective MoS2/PVP, J. Colloid Interface Sci. 630 (2023) 742–753.
[58] X. Bai, et al., Synergy removal of Cr (VI) and organic pollutants over RP-MoS2/rGO photocatalyst, Appl. Catal. B Environ. 239 (2018) 204–213.
[59] S. Li, et al., S-scheme MIL-101(Fe) octahedrons modified Bi2WO6 microspheres for photocatalytic decontamination of Cr(VI) and tetracycline hydrochloride: synergistic insights, reaction pathways, and toxicity analysis, Chem. Eng. J. 455 (2023) 140943.
[60] S. Li, et al., MIL-101(Fe)/BiOBr S-scheme photocatalyst for promoting photocatalytic abatement of Cr(VI) and enrofloxacin antibiotic: performance and mechanism, Chin. J. Catal. 51 (2023) 101–112.
[61] R. Yuan, et al., Self-assembled hierarchical and bifunctional MIL-88A(Fe) @ZnIn2S4 heterostructure as a reusable sunlight-driven photocatalyst for highly efficient water purification, Chem. Eng. J. 401 (2020) 126020.
[62] D. Barpuzary, et al., Noble metal-free counter electrodes utilizing Cu2ZnSnS4 loaded with MoS2 for efficient solar cells based on ZnO nanowires co-sensitized with CuInS2–CdSe quantum dots, J. Mater. Chem. A 3 (27) (2015) 14378–14388.
[63] P. Thammaacheep, et al., Modification of Co3O4/CuBi2O4 composite for photocatalytic degradation of methylene blue dye, Desalin. Water Treat. 267 (2022) 283–292.
[64] X. Yue, et al., Well-controlled SrTiO3@ Mo2C core-shell nanofiber photocatalyst: boosted photo-generated charge carriers transportation and enhanced catalytic performance for water reduction, Nano Energy 47 (2018) 463–473.

[65] F. Yang, et al., Preparation of Z-scheme CuBi2O4/Bi2O3 nanocomposites using electrospinning and their enhanced photocatalytic performance, Mater. Today Commun. 26 (2021) 101735.
[66] D. Gholami, et al., In situ growth of CuFeS2/CuS bridged heterojunction catalyst with mixed redox-couple cations for excellent photocatalytic degradation of organophosphate insecticide: CFD and DFT modeling, Chem. Eng. J. 461 (2023) 141950.
[67] Eshete, M., et al., Charge steering in heterojunction Photocatalysis: general principles, design, construction, and challenges. Small Sci., 2023. 3(3): p. 2200041.